Efficient and stable Ni–Ce glycerol reforming catalysts: Chemical imaging using X-ray electron and scanning transmission microscopy

E. Gallegos-Suárez [a,b], A. Guerrero-Ruiz [b], M. Fernández-García [a,*],
I. Rodríguez-Ramos [a,*], A. Kubacka [a,*]

[a] Instituto de Catálisis y Petroleoquímica, CSIC, C/Marie Curie 2, 28049 Madrid, Spain
[b] Dpto Química Inorgánica, UNED, Paseo Senda del Rey 9, 28040 Madrid, Spain

A R T I C L E   I N F O

A B S T R A C T

Nickel–ceria composite catalysts prepared by a microemulsion method showed outstanding catalytic behavior in hydrogen production by glycerol steam reforming. Contrarily to usual Ni-based catalysts, the system allows long-term stability and nearly absence of by-products, particularly methane and carbon monoxide. With the help of scanning transmission electron microscopy and energy dispersive X-ray spectroscopy we confirmed the key role played by an intimate intermixing of Ni and Ceria components at reaction conditions. In addition, chemical imaging maps as well as more conventional techniques, such as Temperature Programmed Oxidation (TPO) and X-ray Photoelectron Spectroscopy (XPS) were used to identify the carbon containing (including coke) species nature and to establishing their chemical relevance. Combination of these techniques points out that the optimum interphase contact, reached for a specific 20:80 molar Ni:Ce formulation, allows; (i) to keep the Ni particle size controlled with absence of significant formation of coke and thus without deleterious effects on the long-term stability of the catalysts; and (ii) to eliminate undesirable side reactions such as methanation.

1. Introduction

The settlement of a hydrogen economy derived from renewable energy sources may provide significant benefits by solving problems related to the energy crisis and environmental pollution [1,2]. Among numerous renewable candidates, glycerol seems to provide significant advantages. Being a biomass derivative, glycerol is currently produced in large quantities in the process of transesterification of fatty acids into biodiesel [3]. During this process glycerol is normally generated at a rate of 1 mol of glycerol for every 3 mol of methyl ester synthesized, which accounts for approximately 10 wt% of the total product [2,3]. Other bio-based processes also produce glycerol; for example, up to 4 wt% of this molecule (with respect to the initial sugar weight) is obtained in fermentation of sugars oriented to ethanol formation [2]. Due to constant increment of biodiesel production it is estimated that by 2015, 1.54 million tons of glycerol will be generated worldwide [3]. Thus, in order to make the chemicals obtained from the biomass sector competitive with chemicals from fossil fuels, all of this glycerol should be efficiently processed.

Bio-oils including glycerol have numerous potential applications which includes its usage in boilers for heat and electricity, in engines and turbines for electricity, in chemicals production such as phenols, organic acids, and oxygenates or in transportation fuel production [1–3]. The latter would be the more important from a economic point of view, however bio-oil derived transportation fuels require expensive upgrading techniques, and this route is currently less attractive for motor fuels production. To alleviate this disadvantage, reforming of bio-oil has been proposed and employed to produce hydrogen, a key fuel for the future.

The steam reforming of glycerol appears thus as a potential alternative for producing hydrogen in the near future with significant impact in the viability of numerous bio-refining processes [1–4]. Steam reforming of glycerol is an endothermic process and the offgas composition is governed by the (formal) equilibrium between the decomposition, reaction (1), water gas shift (WGS), reaction (2), and methanation, reaction (3) [5]:

$$C_3H_8O_3 \rightarrow 3CO + 4H_2 \tag{1}$$

$$CO + H_2O \leftrightarrow CO_2 + H_2 \tag{2}$$

$$CO + 3H_2 \rightarrow CH_4 + H_2O \tag{3}$$

* Corresponding authors. Tel.: +34 915854939; fax: +34 915854760.
E-mail addresses: mgf@icp.csic.es (M. Fernández-García), irodriguez@icp.csic.es (I. Rodríguez-Ramos), ak@icp.csic.es (A. Kubacka).

The first two provide a H_2/CO_2 ratio of 7/3 which will render the maximum attainable hydrogen yield. The third, methanation, is an almost unavoidable reaction in Ni-based catalysts which can limit such hydrogen yield. High temperatures will shift the decomposition (reaction (1)) and methanation (reaction (3)) steps to enhance production of H_2. This however has concomitant detrimental effects in catalyst lifetime due to the aggregation of the active metals and carbon deposition [2].

In this context the search of active and stable, low-temperature glycerol reforming catalysts is a field of intense research [2]. Ni-based catalysts are among the best choices for the reaction not only from a catalytic but also from a economic point of view, due to its significantly lower price than other, alternative active metal typically used in this reaction, i.e. Pt [1,2]. Both metals, Ni and Pt, are active in dehydrogenation and decarbonylation reactions to produce hydrogen although Ni shows enhanced activity toward methanation. Enormous efforts have been made in Ni-based systems to control activity/selectivity in reforming reactions to favor hydrogen production, and to increase the resistance to carbon formation and sintering of the metal phase. Strategies related to regulating surface composition, tuning particle sizes and shapes, metal "encapsulation" by rigid supports, enhancing metal–support interaction, and fabricating hierarchical structures within the catalysts has been essayed with partial success [6–24].

In this contribution we exploit the development of a Ni–CeO$_2$ catalyst system based in a single pot preparation method yielding a fluorite-based mixed oxide. This system has been shown high activity in the WGS and ethanol reforming reactions as it evolves in a "composite" metal–oxide (nickel–ceria) solid with high interaction area among components [8,25]. In this work, we subjected such system to the more thought glycerol reforming test and founded superior performance in terms of activity/selectivity and stability. Specific nickel–ceria formulations having certain Ni/Ce atomic ratios show activity at relatively low temperatures, e.g. well below 873 K, and presents significant stability under reaction conditions due to the control of the structure/morphology of the solid-state components of the system as well as of the carbon formation process. To interpret the scientific bases of these features at atomic scale we present a scanning transmission electron imaging study with the aim of "chemically" discriminating between elements of the samples [26]. To this end, energy dispersive X-ray maps were obtained for a series of catalysts to track the evolution of metal, oxide and carbon phases present in spent catalysts. Combined with more conventional techniques such as X-ray diffraction, X-ray photoelectron spectroscopy and temperature programmed oxidation reaction, we would provide evidence of the key issues leading to highly active and stable Ni-based glycerol reforming catalysts.

2. Experimental

The Ce–Ni composite catalysts were prepared by employing reverse microemulsions following using *n*-heptane (Scharlau) as organic media, Triton X-100 (Aldrich) as surfactant and hexanol (Aldrich) as cosurfactant. Ce and Ni nitrates (Aldrich) were used as metal precursors [25]. Water/M (M = Ce + Ni) and water/surfactant molar ratios were, respectively, 110 and 18 for all Ce–Ni samples as well as a CeO$_2$ support reference. Systems are called Ni20 and Ni30 in correspondence of the molar percentage of Ni on cationic basis (equivalent to a 7.7 and 12.3 wt% of metallic Ni, respectively) as measured by X-ray Total Reflection Fluorescence (error below 3%). For the Ni20/CeO$_2$, the nickel nitrate has been used to impregnate the ceria support with the same loading as the Ni20 sample. Samples were dried overnight as subsequently calcined at 773 K during 2 h. Prior to reaction, samples were pre-reduced in 10%

H_2/He at 773 K during 2 h. For analysis (see below) of samples after reduction, they were transferred to the characterization technique cells in contact with air.

The BET surface area and average pore volume values were measured by nitrogen physisorption (Micromeritics ASAP 2010). XRD profiles were obtained with a Seifert D-500 diffractometer using Ni-filtered Cu $K\alpha$ radiation with a 0.02° step and fitted using the Von Dreele approach to the Le Bail method [27]; particle sizes and microstrain were measured with XRD using the Willianson–Hall formalism [28].

TEM analyses were done using a JEOL 2100F field emission electron gun microscope operated at 200 kV and equipped with an Energy-Dispersive X-Ray detector. The sample was ground until powder and a small amount was suspended in ethanol solution using an ultrasonic bath. Some drops were added to the copper grid (Aname, Lacey carbon 200 mesh) and the ethanol was evaporated at room temperature before introduce in the microscope. The Scanning Transmission Electron Microscopy (STEM) was done using a spot size of 1 nm.

The Temperature Programme Oxidation (TPO) analyses were done in a SDTQ600 5200 Thermogravimetric Analysis system. In this latter, the samples were heated from room temperature to 1173 K, with a heating rate of 8 K/min under pure air.

X-ray photoelectron spectra of the used samples were recorded with an Omicron spectrometer equipped with an EA-125 hemispherical electron multichannel analyser and X-ray source (Mg $K\alpha$) operated at 150 W, with pass energy of 50 eV. Each sample was pressed into a small pellet of 15 mm diameter and placed in the sample holder and fixed with a gold grid. The sample was degassed in the chamber for 6–8 h to achieve a dynamic vacuum below 10–8 Pa before analysis. The spectral data for each sample was analyzed using CASA XPS software. The Au 4f7/2 peak at 83.4 eV was used as an internal standard.

The glycerol steam reforming was conducted in a stainless steel fix-bed reactor (Length: 47 cm; inner diameter: 0.95 cm), operating at atmospheric pressure. The reactor was filled with 30 mg of catalyst and SiC was added to obtain 4 cm length. Prior to the catalytic test, the catalyst was reduced over 1 h with H_2 flow at 673 K increasing the temperature at 5 K/min. When the catalyst was reduced 50 mL/min of N_2 flow through the reactor and a mixture of 10 wt% (2.1 mol%) of glycerol in water (1 g/h) was added using a Controller Evaporator Mixture (CEM) (Bronkhorst) working at 473 K. After the CEM, all the system was heated to prevent condensation until the cooling system situated in the reactor exit. The outlet gas was analyses online with a GC equipped with two thermal conductivity detectors and one flame ionization detector (Bruker GC-450). The reaction test with water was done using the same experimental conditions and after reaction, the feed was changed to introduce 1 g/h of pure water.

For thermodynamic equilibrium calculations we used the Aspen-Hysys software. The Gibbs reactor was used to calculate the product composition behavior vs. temperature and other experimental variables using the condition of minimization of Gibbs free energy and the Peng–Robinson state equation due to its largest applicability range in terms of temperature, pressure and also because its suitability for systems containing hydrocarbons, water, air and combustion gases [29].

3. Results and discussion

The glycerol steam reforming activity of the Ni–Ce composite catalysts having 20 and 30 mol. Ni % on cation basis (called Ni20 and Ni30) and a reference Ni supported on CeO$_2$ (called Ni20/CeO$_2$) having the exact molar composition of the Ni20 catalyst were tested at 773 K. After stabilization on stream, the H_2/CO_2 ratio is 7/3 (within ±8%) for the two composite materials indicating that
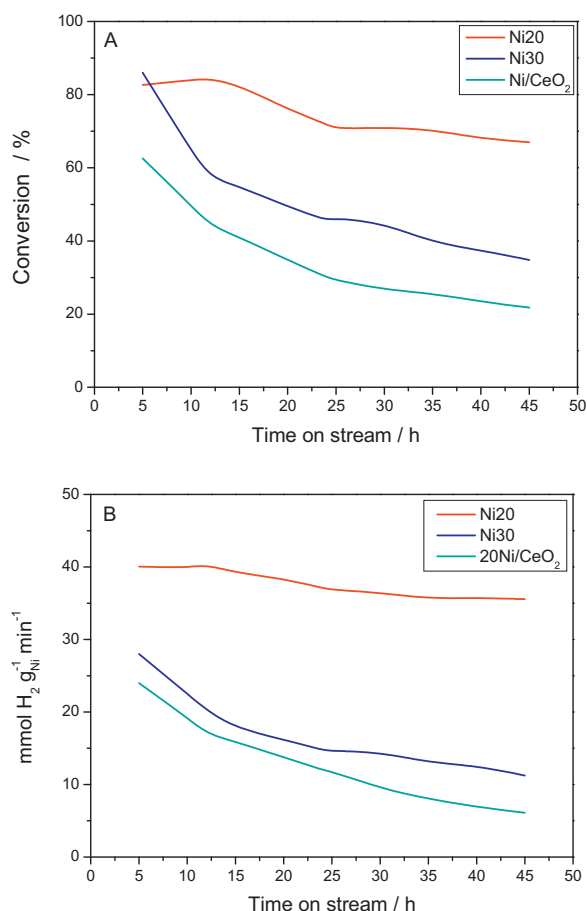
Fig. 1. Glycerol reforming conversion (A) and hydrogen molar activity per gram of Ni (B) vs. time on stream for the Ni (Ce samples.

both composite catalysts convert glycerol using an overall reaction close to:

$$C_3H_8O_3 + 3H_2O \rightarrow 3CO_2 + 7H_2 \qquad (4)$$

Only trace amounts of additional products were observed (see below). Stable conditions over an extended period of time (ca. 48 h) were obtained at 773 K. We thus provide a first comparison of the samples at this temperature using two observables, the conversion of glycerol (panel A) and the hydrogen molar yield (panel B) in Fig. 1 while a more detail analysis of carbon-containing gas-phase products is presented in Fig. 2.

The time on stream performances of the Ni20 and Ni30 catalysts, as well as the sample Ni20/CeO$_2$, are displayed in Fig. 1. In the catalytic runs presented in this figure, conversion was kept below 99% (thermodynamic equilibrium) but sufficiently high to obtain information about deactivation. The performance of the composite catalysts is clearly better than the one displayed by the two-phase, impregnated catalyst.

Both composite catalysts achieve hydrogen yields per mol of glycerol reasonably close to the maximum possible (i.e. 7 mol per mol of reactant) after a few hours from the beginning of the reaction, maintaining such value (very slow decay as can be interpreted from Fig. 2; see below) in certain cases throughout the whole experiment. Hydrogen production is, in the Ni20 case, close to the thermodynamic equilibrium of the reaction mixture as it would render an almost selective hydrogen production (98.8%) with rather minor presence of methane as hydrogen-containing product. The maximum or optimum yield of hydrogen per mol of glycerol is usually reached at higher temperatures, over 823 K, in Ni-based catalysts [17,30–33]. For the specific case of ceria-promoted catalysts
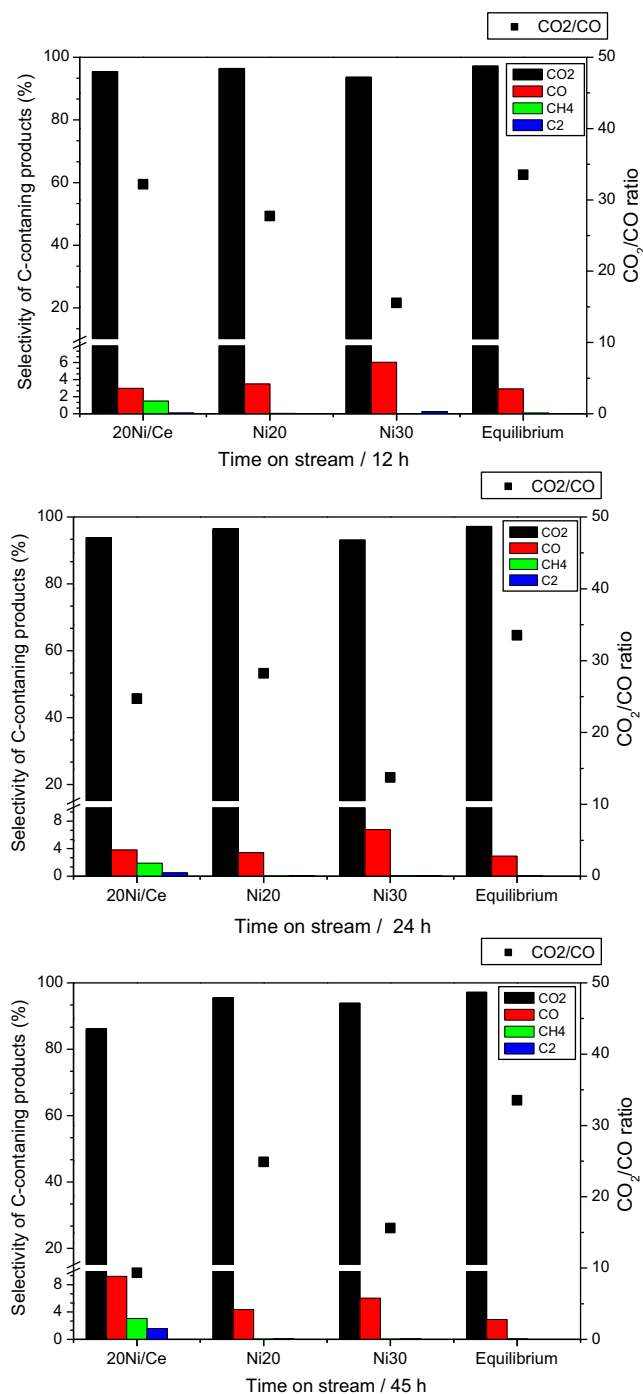
Fig. 2. Selectivity of C-containing species gas-phase products for the samples and corresponding thermodynamic equilibrium values for the reaction mixture.

and at the operation temperature of our experiment, hydrogen production presents important shortcomings in previously published works: optimum hydrogen yield is either obtained at 873 K [32,33], or below that temperature the production of hydrogen is far from optimum as an effect of the poor selectivity control with significant formation of a number of hydrogen-containing products such as methane and C1–C2 oxygenates [32].

Focusing on comparing now our composite samples, the activity of the Ni30 sample is lower than the one of Ni20 and, moreover, shows a temporal behavior relatively similar to the Ni20/CeO$_2$ sample, indicating that the Ni30 sample has certain similarities with a normal, impregnated ceria-based nickel sample. Still its activity is
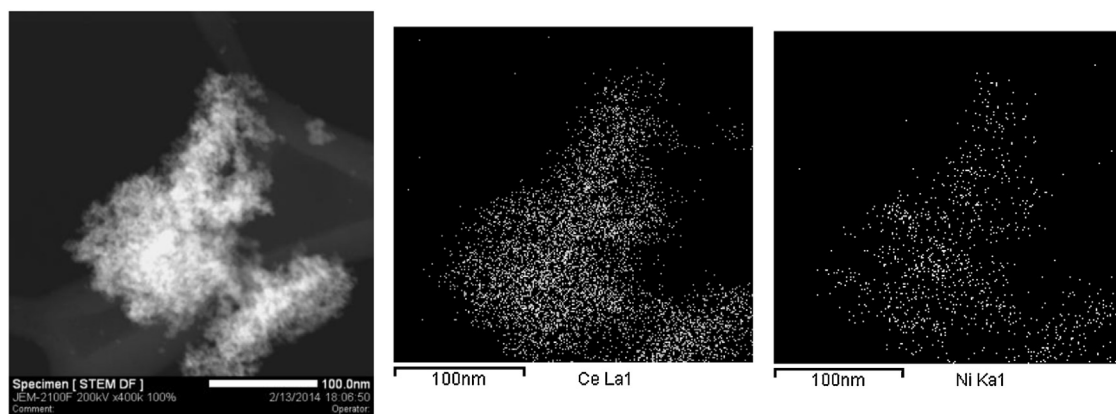
Fig. 3. STEM micrograph and corresponding Ce and Ni chemical maps of the pre-treated (reduced) Ni20 sample.

higher than the Ni20/CeO$_2$ for all times essayed. In any case, the optimum activity and selectivity is achieved with the Ni20 sample. This sample presents a behavior significantly different from impregnated samples as the reference (Ni20/CeO$_2$) used here or those presented in the literature [17,18,30,32,34,35].

To show this in more detail, the distribution of C-containing products is presented at specific reaction times in Fig. 2. The results of the thermodynamic calculation described in Section 2 are also included in this figure. CO$_2$/CO molar ratios above 25 are always observed for Ni20 while such ratio decreases up to ca. 15 for the Ni30 case. Both ratios are outstanding ones if compared with Ni-based systems reported in the literature [17,32,33]. The plot in Fig. 2 also shows that this ratio is not stable for the Ni20/CeO$_2$ material.

In fact, as occurring in many cases in the literature, this Ni20/CeO$_2$ catalyst does show selectivity evolution with additional production of C2 hydrocarbon chains at time-on-stream values above 24 h. As well known ethylene and other olefins polymerize at the catalyst surface and are initiators of highly detrimental coke [17,32]. We can also note that a relatively low formation of CO is positive in terms of significant coke production as it is well known that a low temperature (below 873–923 K) path for coke formation is the Boudouard reaction [34]. The absence C$_2$–C$_3$ oligomers in addition to the relatively low CO production seem thus elements supporting the good selectivity and stability of the Ni20/Ni30 catalysts.

Summarizing, Fig. 2 provides evidence of the control of CO, CH$_4$ and other side molecules production in the composite catalysts
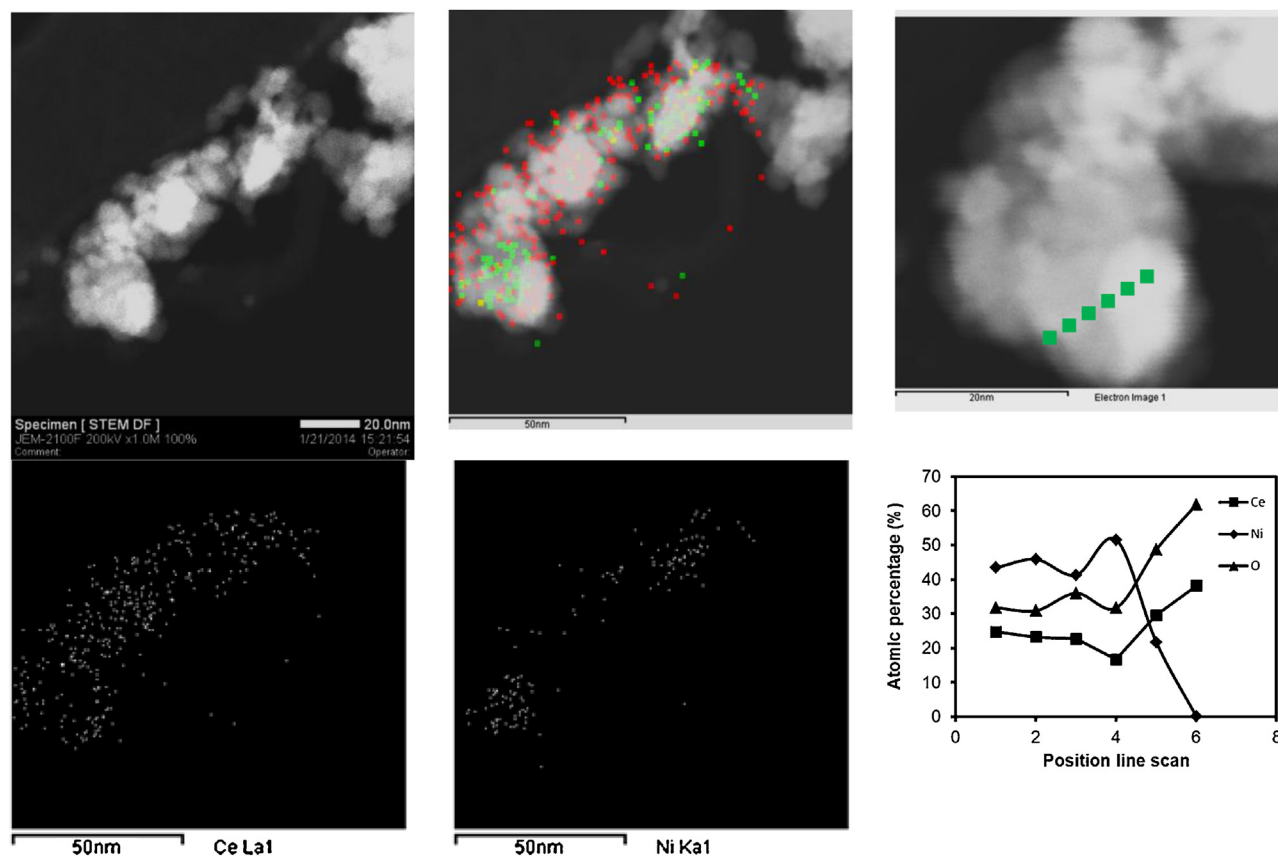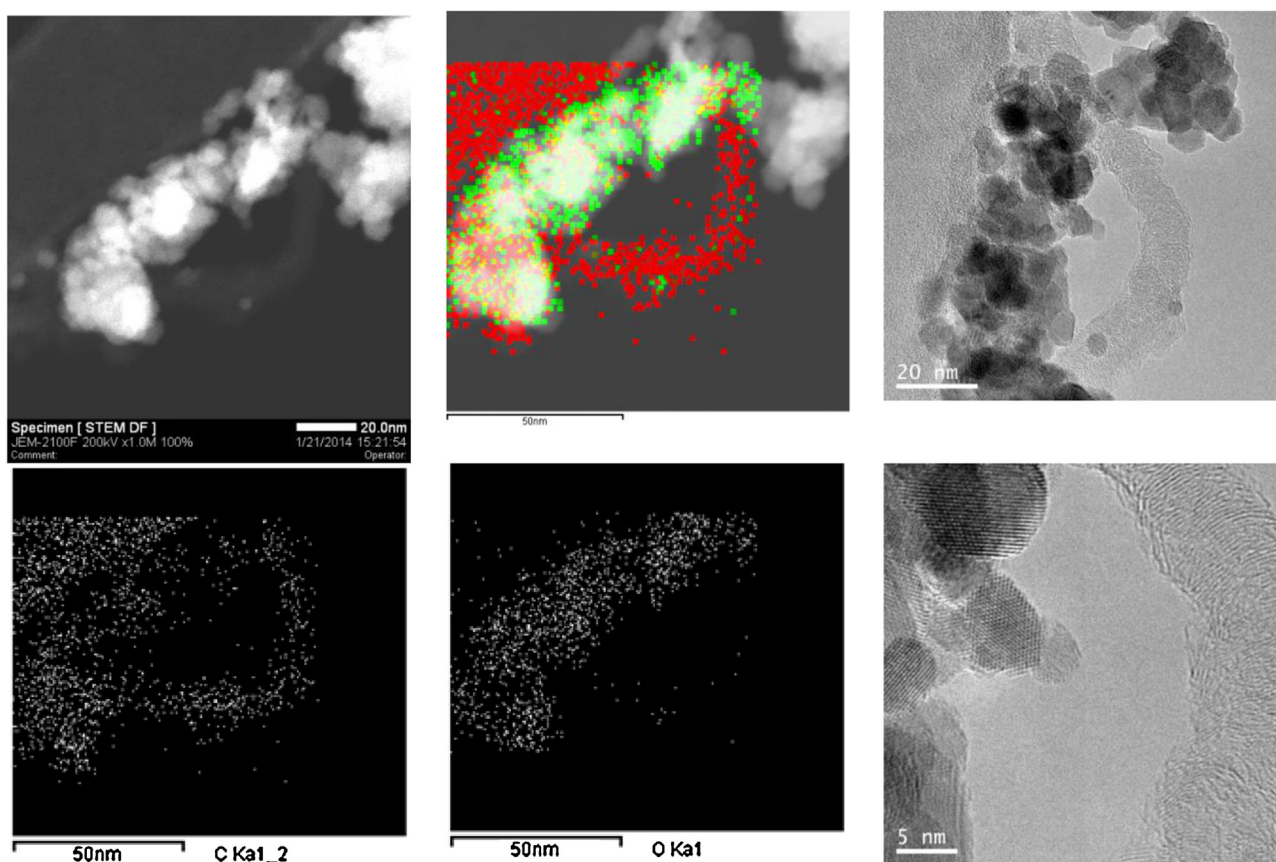

Fig. 4. STEM micrograph and corresponding Ce (red), Ni (green) and overlaying (Ce–Ni) chemical maps of the Ni20 sample after reaction. The result of an EDXS line scan is also presented. (For interpretation of the references to color in text, the reader is referred to the web version of this article.)

Fig. 5. STEM micrograph and corresponding C (red), O (green), and overlaying C—O chemical maps of the Ni20 sample after reaction. Two TEM micrographs are also presented for the same zone at two magnifications. (For interpretation of the references to color in text, the reader is referred to the web version of this article.)

and particularly in Ni20. Although the mechanism of the glycerol reforming is not fully elucidated, there are indications that methane and small hydrocarbons are formed by hydrogenolysis (leading to simple alcohols such as methanol as key intermediates) or by dehydratation and further hydrogenation (from hydroxyacetone as key intermediate further evolving in acids such as acetic and formic) [36–38]. The dehydration pathway is usually important in acid systems and may not be thus a prevalent route in the case of ceria-based materials. In Ni-based materials, the well-known strong activity in methanation also appears as a significant pathway for methane formation [2]. While the almost null activity in methanation of the composite materials was previously proved [8], the results in Fig. 2 shown that both methane formation paths above mentioned are efficiently controlled in Ni20. Similarly, CO production is rather low, in this case, likely as an effect of the rather important water gas shift activity owned by ceria-related catalysts. This has been previously demonstrated for the particular case of the Ni20 material [25]. In our composite catalysts, the overall catalytic performance is controlled by the chemical/oxidation state of the metal and the metal–support interaction. The latter controls the active state of the metal at the interphase between the two components as well as the oxide vacant role in the activation of oxygen-containing molecules [2,8,32,33]. The adequate combination of catalytic properties and, as detailed below, the intimate contact between nickel and ceria would thus provide the basis for the good selectivity performance observed for Ni20, rendering a product distribution rather close to the thermodynamic equilibrium result (Fig. 2).

To interpreting the outstanding catalytic properties of the Ni20 sample, we carried out a scanning transmission electron microscopy (STEM) study of the composite catalysts. As an illustrative example of the state of the materials after reduction pre-treatment Fig. 3 displays the Ni20 case. The reduction of the composite catalysts has been examined previously using spectroscopic techniques, proving key information about the presence of metallic nickel and oxidic ceria (fluorite-type) phases [25]. Here the STEM and chemical mapping images highlights the reasonable chemical homogeneity of the Ni dispersion on the fluorite-type ceria matrix. Ni is barely seem by XRD in the reduced catalysts (small peak near 50 degrees) while the fluorite-type ceria phase is clearly visible with a primary particle size of ca. 5 nm (see Fig. S1 and Table S1 at the supporting information section). We employed microscopy to analyze the Ni-based catalysts after reduction. Due to the strong intermixing of the components, inherent to the preparation method (where Ni metal and Ceria oxide evolve from a single phase), and the presence of Ni in all surface and bulk (and not only in the former) parts of the material, we focus on using chemical mapping tools as the optimal analytical choice. Thus the average nickel aggregate size was estimated from STEM chemical mapping, yielding an aggregate size of 3.4 and 4.3 nm for, respectively, Ni20 and Ni30 samples (see Table 1).

Table 1
Average particle size (first raw order moment), variance (second raw order moment) and higher normalized central moments of Ni aggregates in the Ni20 and Ni30 catalysts. See text for details.

| Sample	Size (nm)	Variance (nm^2)	Skewness (a.u.)	Kurtosis (a.u.)
Ni20 red.	3.4	1.0	0.6	0.2
Ni20 used	3.8	1.3	0.4	0.6
Ni30 red.	4.3	3.1	0.8	0.6
Ni30 used	7.8	15.3	1.2	1.0$_5$
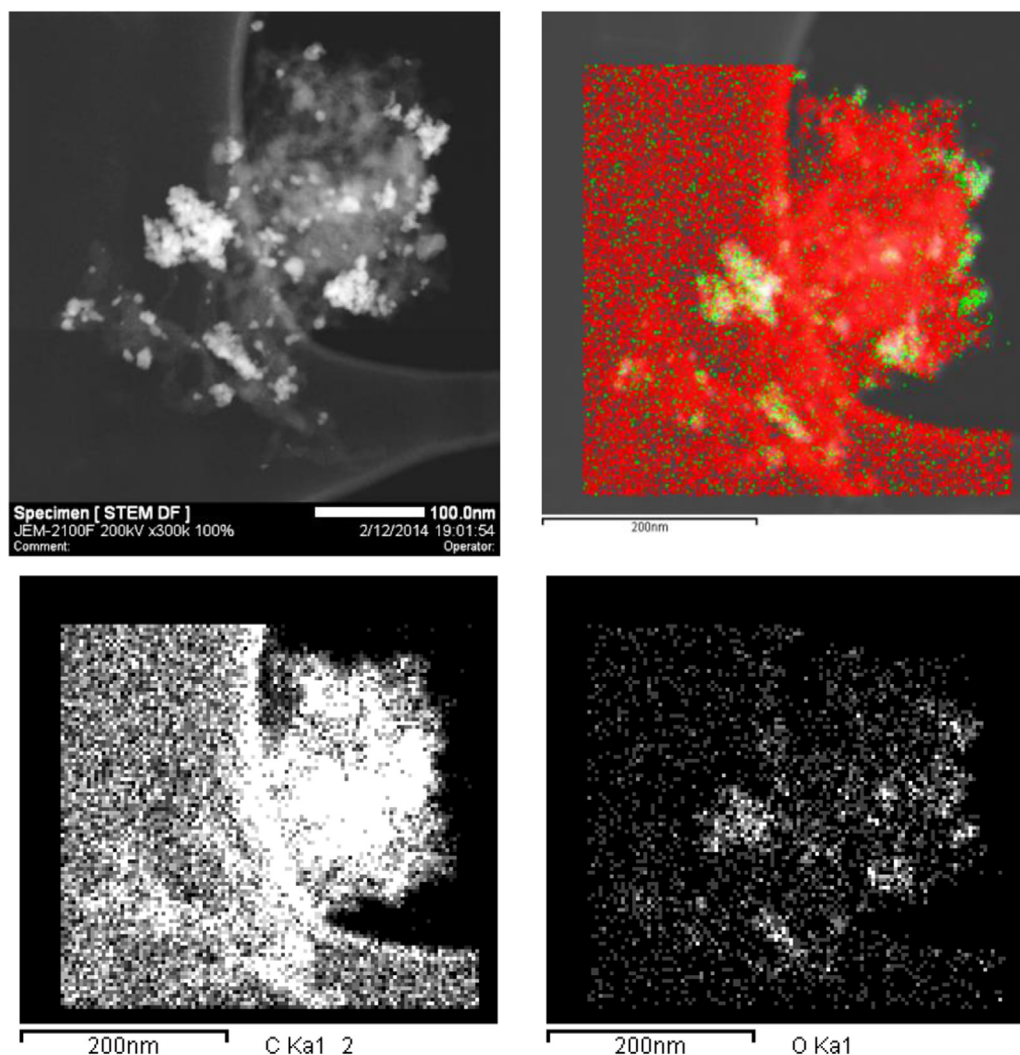
Fig. 6. STEM micrograph and corresponding C (red), O (green), and overlaying C—O chemical maps of a second aggregate of the Ni20 sample after reaction. (For interpretation of the references to color in text, the reader is referred to the web version of this article.)

After ca. 48 h of reaction the chemical heterogeneity of the materials increases significantly. For the Ni20 sample this is illustrated in Figs. 4–6. In Fig. 4 we present chemical maps displaying the location of ceria and nickel after reaction, together with the micrograph image from which they were taken. The chemical map shows the presence of ceria and nickel rich zones, in contrast with the more homogeneous situation displayed in Fig. 3. To make a more quantitative analysis, a line profile analysis is also included in Fig. 4. Overall, the zone is nickel-enriched with respect to the chemical composition obtained by chemical analysis (Ni:Ce average atomic relation ca. 3:2 instead of the 1:4 of the material). The uphill line goes from zones with high Ni:Ce ratios near 2 to those near zero. This illustrated the rupture of the nickel-ceria contact expected during reaction in a zone were the intensity of such process appears maximum [8]. Still, the ceria-rich parts show presence of Ni in more than 95% from individual energy dispersive X-ray spectra (EDXS). As these are taken with a 1 nm beam, it clearly shows that contact between the two components is still present at subnanometric level. Specifically, particle size estimation using chemical mapping STEM tools (using Figs. 4 and 6 as well as Fig. S2) indicates that Ni aggregates grow for Ni20 and Ni30 cases under reaction but to a significantly lower extent in the former case (see Table 1). While the analysis presented in Table 1 is not considered fully quantitative as, among several factors, it is difficult to distinguish between

Ni aggregates from Ni present at ceria lattice (we assigned arbitrarily signals below 1.5 nm to lattice entities), the distribution moment values displayed in Table 1 and more precisely, the differences between pre-treated (reduced) and used samples, provide a reasonable quantification of the "disproportion" evolution taking place between the two Ni and Ce components from the pre-reduced solid to the specimen after reaction conditions. For Ni20, Table 1 points out that the Ni aggregate distribution shows strong analogies in the fresh (after reduction) and used (after reaction) states. The control of Ni dispersion and particle size (more generally speaking, morphological properties) has been shown critical to obtain high hydrogen yields through the control of glycerol decomposition handling and water gas shift activity enhancement [15,17,39]. Worth to mention is the fact that analysis of Ni by other bulk averaged techniques like XRD or EXAFS are relatively less informative in this situation where a complex distribution of the active metal takes place throughout the existent phases. This in addition to strong limitations in their in situ capabilities; to our knowledge no single in operando experiment has been reported in gas phase glycerol reforming due to the high boiling point and viscosity of the reactive.

Fig. 5 shows analogous data (to Fig. 4) for location of carbon-containing deposits. This figure also presents a normal TEM image at two magnifications. In the latter presence of filamentous
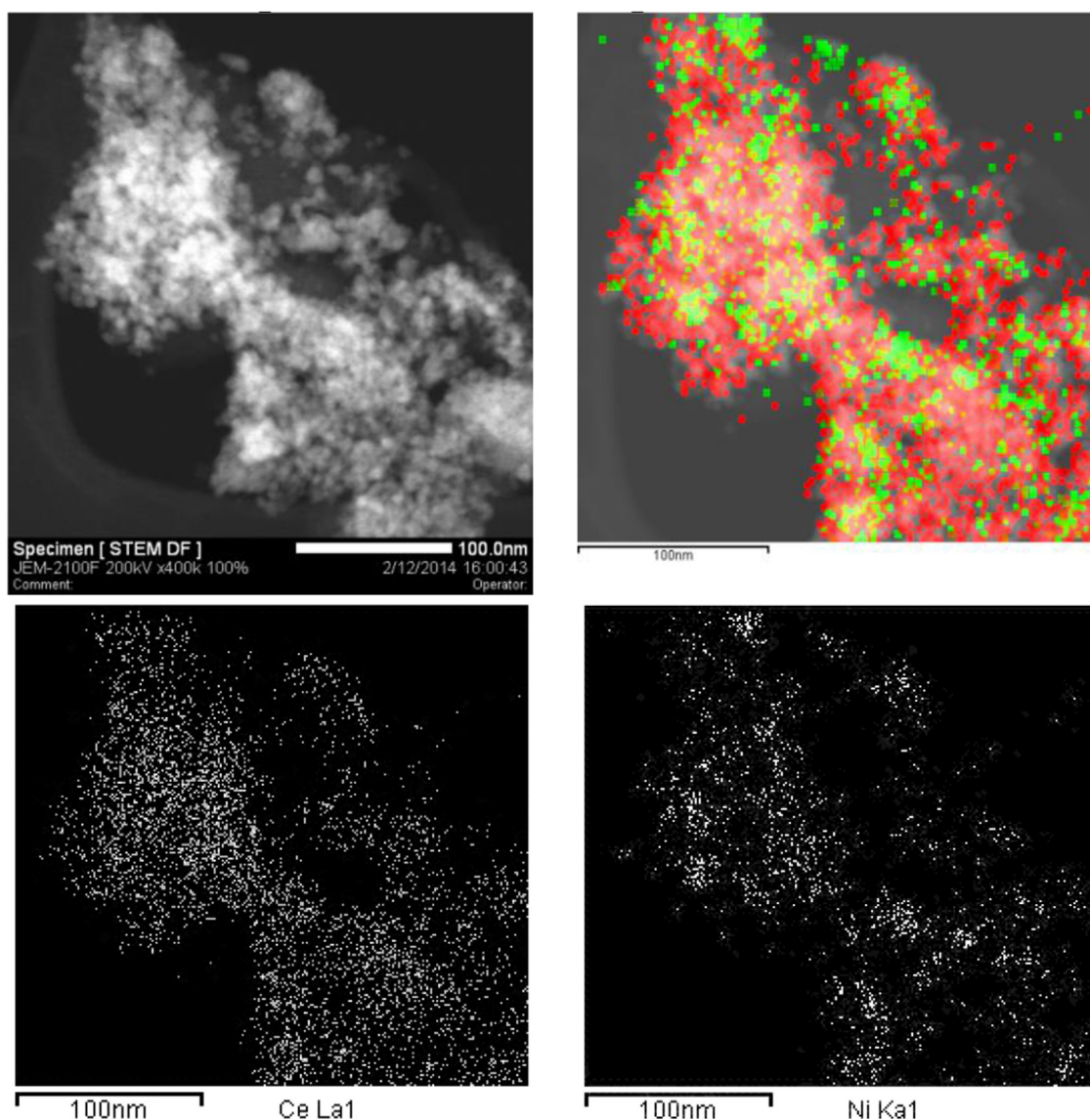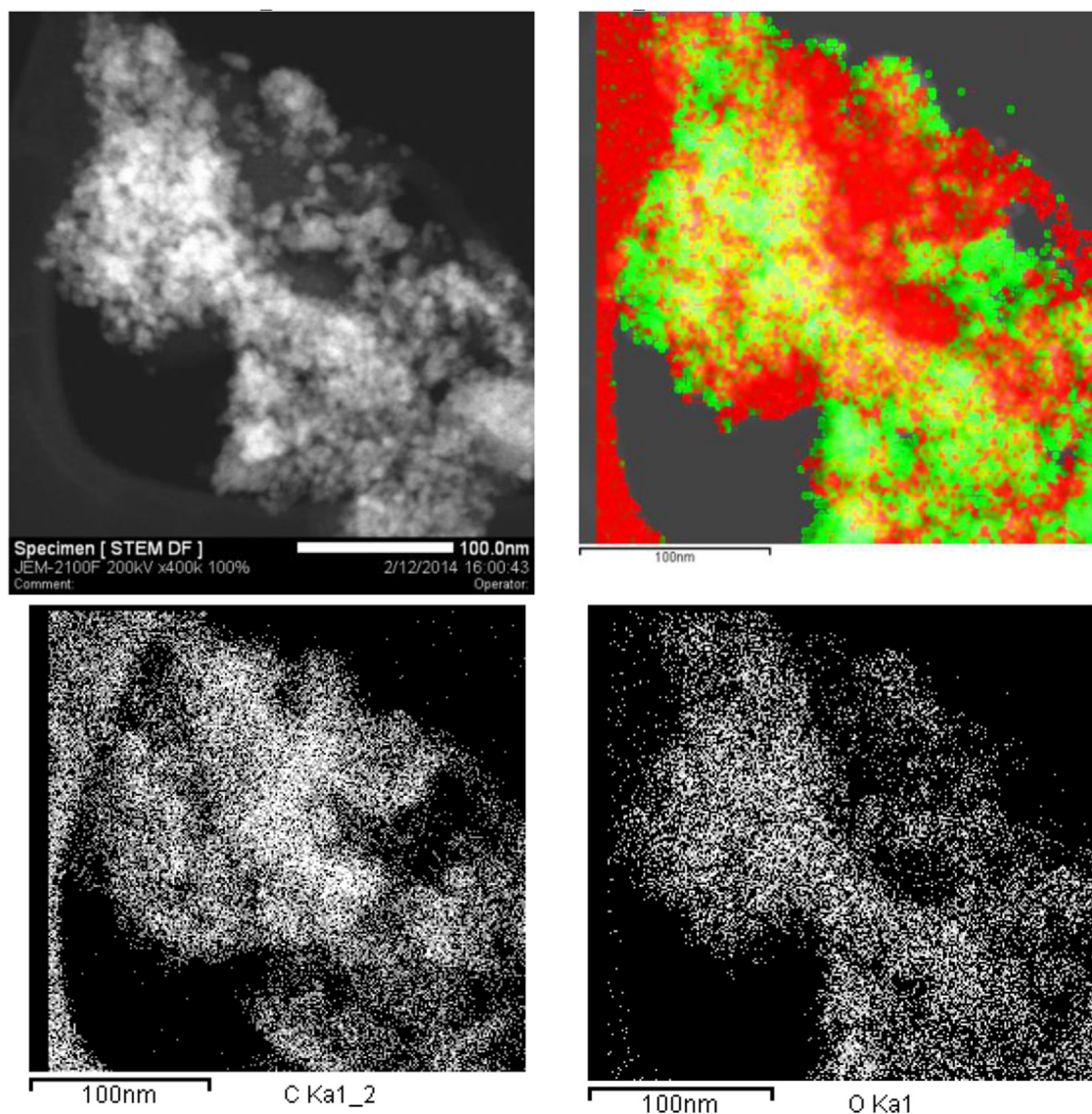
Fig. 7. STEM micrograph and corresponding Ce (red), Ni (green), and overlaying Ce–Ni chemical maps of the Ni30 sample after reaction. (For interpretation of the references to color in text, the reader is referred to the web version of this article.)

carbon is observed [40,41]. Such carbon structure presents some ill-organized growth with layered graphitic walls in perpendicular direction to that of the growth direction. The presence of such type of carbon structure is relatively low, on average less than 5 on ca. 10^4 nm^2. Moreover, the information enclosed in the mapping indicates that a significant part of carbon is still located near the catalysts, without forming nanofiber or any other typical nanoarchitecture of carbonaceous materials. Fig. 6 better illustrates the nature of such carbon in intimate contact with the catalyst. In this figure, a cloud of carbon-containing material is surrounding the mixed nickel–ceria entities. Overlaying of the C and O EDXS chemical maps show that this type of carbon deposit contains oxygen to an important level. So, it is expected to be a highly hydrogenated, truly amorphous carbon-containing component with chemical composition far from coke and thus with absence of strong deactivation effects over the catalyst.

Figs. 7 and 8 attempt to illustrate the situation for the Ni30 sample. In Fig. 7 (and Fig. S2) the overlaying of the nickel and cerium EDX maps show a significantly larger clustering effect, providing a clear clue toward the lower contact between the two phases

present in the catalyst under reaction. The important growth of the mean and variance of the Ni aggregate size distribution in going from the pre-treated (reduced) to the final (after reaction) samples supports quantitatively this conclusion (Table 1). The system however, presents evidence of carbon containing species with similar C and O overlaying effects (Fig. 8; upper part) as observed for the Ni20 case. Nevertheless, Fig. 9 shows the existence of a new carbon-containing species; in this case we can see numerous filamentous (some of them hollow core) carbon with nickel particles (according to EDXS analysis) at the end. As it shows the last image of Fig. 9 such fibers grow from the solid but separate the metal definitively from ceria. As well known, this is a major concern with regard to the coverage of the active metal sites by carbon species that can lead to deactivation of catalysts in reforming reactions [40–45]. The initial quantity or loading of nickel in the catalysts would thus control the average particle size of the metal during reaction. Those particles of larger particle size and, consequently, with limited interaction with the support, are finally producing C carbon fibers which encapsulates the metal. While nickel in Ni20 would have a minimum fraction of the metal in such condition, a

Fig. 8. STEM micrograph and corresponding C (red), O (green), and overlaying C—O chemical maps of the Ni30 sample after reaction. (For interpretation of the references to color in text, the reader is referred to the web version of this article.)

noticeable fraction is observed at Ni30. Such issue is responsible of the deactivation decay observed in Fig. 1 while the remaining nickel in contact with ceria is providing the stable activity observed at large reaction time on stream.

We can thus observe that Ni20 and Ni30 have nickel entities differing essentially in the parts where the contact between nickel and ceria components is lost. The preparation method of the samples thus provides a way to stabilizing the nickel–ceria interface which is fully operative in the Ni20 catalyst. Above that, the excess of nickel allows a behavior typical of the supported catalysts with carbon structures occluding the active nickel phase at relatively long time on stream, resulting in the strong deactivation profile
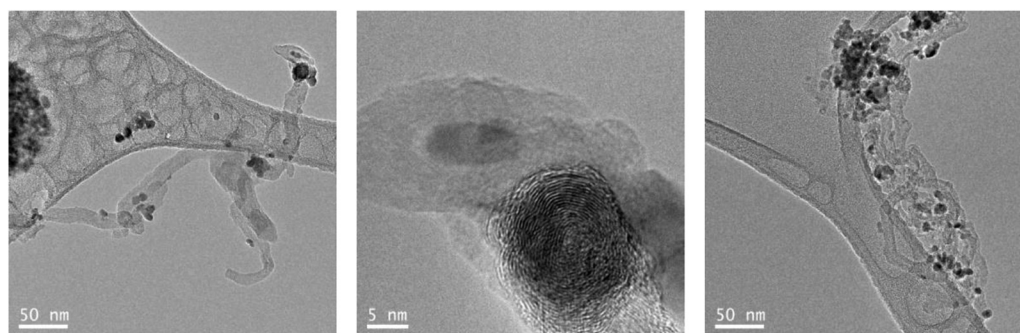
Fig. 9. TEM micrographs of the Ni30 sample showing zones with presence of Ni and C structures.

Table 2
Summary of carbon content and C species percentage over total carbon as determined by TPO experiments over used (after reaction) samples. See text for details.

Sample	Glycerol-type (423–673 K)	Graphitic (673–1173 K)	g_{carbon}/g_{cat}
Ni20	69	31	0.040
Ni20-w	13	87	0.018
Ni30	15	85	0.057

presented by Ni30 in Fig. 1. Note that as summarized recently in the review of Tran et al. [2] the maintenance of the metal–oxide interface in ceria-based systems is critical to hold high activity, particularly in relation with the presence of oxygen vacancies at the interface and the promoting effect on water activation and water gas shift reaction and on the suppression of the methanation process. As previously discussed, both facts are capital to end up in the control of gas phase products and to provide a "stable" behavior as shown in Figs. 1 and 2. The microscopy study indicates that the significantly developed nickel–ceria interaction coming directly from the preparation method and its stability under reaction has a direct consequence in controlling the carbon-containing phases produced (Figs. 5, 6, 8 and 9) as well as the control of growth processes in both nickel (see Table 1) and ceria (Fig. S1 and Table S1 at supporting information) phases. The Ni20 sample study thus indicates that the progression of carbon phases is stooped with production of carbon-containing hydroxylated phases which can evolve in the reaction products ($CO_2 + H_2O$) easily. In parallel, Ni aggregates suffer a rather mild growth process during 48 h of reaction (see distribution moment values at Table 1) as a consequence of the stabilizing effect of the ceria contact.

We carried out a simple chemical test to proof the behavior of the highly hydroxylated carbon species by subjecting the spent Ni20 catalyst to water treatment at reaction conditions (e.g. in absence of glycerol, maintain all other experimental reaction variables). The sample after this test was called Ni20-w.

Using Ni20, Ni20-W, and Ni30 we use temperature programmed oxidation (TPO) and X-ray photoelectron spectroscopy (XPS) to further characterize the carbon containing species already analyzed by microscopy. A summary of the TPO results is presented in Table 1 while a representative example of the experimental results in shown in Fig. S3 of the supporting information. Table 1 summarizes the contribution of the two main peaks observed in the Derivative TPO profiles. A low temperature peak, which according to its maximum will content glycerol (boiling point at 543 K) and similar small molecules or oligomers, appears as the main component for Ni20 (Table 2). Contrarily, the carbon containing species oxidized at higher temperature dominates in the Ni20-w and Ni30 cases. Such species, evolving above 673 K are usually described as graphitic (see below). More importantly, the TPO experiment shows that the water treatment is able to convert highly hydroxylated carbon species in evolving gases and leaves the graphitic-type at the surface. The latter, graphitic-type species dominates the Ni30 case. The different nature of the post-reaction carbon species are thus in agreement with the microscopy analysis.

To further analyze this point, we also carried out a XPS study. Results for the C 1s XPS peak are depicted in Fig. 10. A Summary of the C 1s contributions binding energy and relative abundance
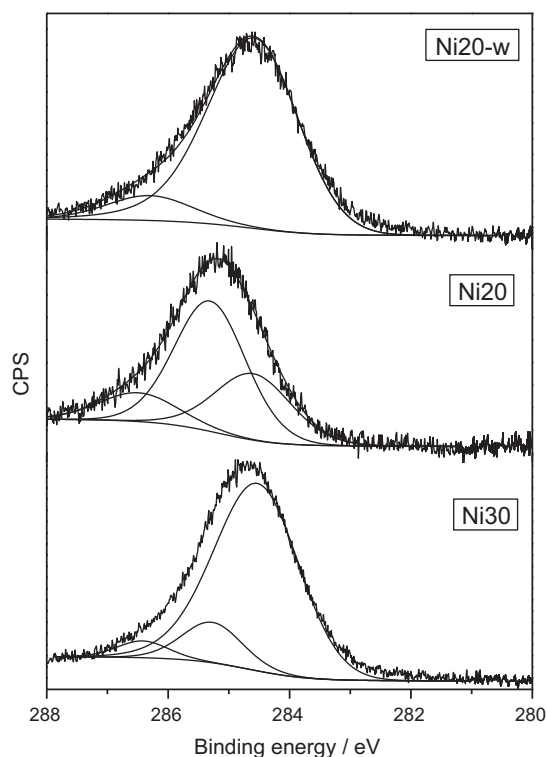
Fig. 10. C 1s XPS peak of the Ni20, Ni20-W, and Ni30 samples after reaction.

(%) is presented in Table 3. Three species are detected and correspond to carbon species with dominant sp2 (ca. 284.6 eV), sp3 (ca. 285.3 eV) electronic character, as well as those with an environment described as C—O bonds (ca. 286.4 eV) [46–48]. The first contribution mentioned is customarily assigned to graphitic-type deposits. In the context of our work, the second one at 285.3 eV is assigned to hydrogen incorporated carbon species [46,48].

The joint analysis of Tables 2 and 3 would thus support the conclusions extracted from the microscopy study. An increase of Ni content in the composite catalysts increases the contribution of the carbon species more resistant to chemical oxidation and displaying a graphitic-type chemical identity. This is a direct consequence of the decreasing Ni–Ce interaction uncovered by the STEM–EDXS chemical imaging analysis. In the Ni20 case, oligomeric, hydroxylated carbon species dominates according to these two techniques. A similar conclusion can be extracted from the Ni20-w test carried out. In an optimum catalyst, this Ni–Ce interaction prevents the Ni growth and encapsulation by carbon species (effects occurring in Ni30; Fig. 9) and the concomitant irreversible deactivation. The Ni20 sample does not suffer these effects by maintaining the interaction between the two main phases of the system, metallic Ni and oxidic ceria, with an efficient supply of oxygen–hydrogen species to the initially formed carbon residues. The outstanding properties of the system derived from the strong interaction between the two main components and affecting the glycerol decomposition are completed with both high water gas shift and low methanation activities [8,25], providing a rather good system with limited

Table 3
C 1s XPS peak analysis of the used (after reaction) samples. See text for details.

Sample	Binding energy (eV)			Relative C1s peak area (%)		
	Csp^2	Csp^3	C—O	Csp^2	Csp^3	C—O
Ni20	284.6	285.3	286.5	30	56	14
Ni20-w	284.6	–	286.3	88	–	12
Ni30	284.5	285.3	286.4	82	13	5

production of CO and CH$_4$ by-products (Fig. 2). These outstanding catalytic characteristics of the Ni20 material, mainly high activity and stability as well as significant absence of by-products, have not been presented to our knowledge in the literature [5,9,17,18,30,32], giving clear indications of the exceptional behavior of this catalyst in the reforming of glycerol, a challenging reaction.

4. Conclusions

Using a microemulsion procedure we synthesized Ce–Ni mixed oxides having fluorite-type structure. Following reduction and under reaction conditions, evolve forming separate Ni–metal and Ce–oxide phases. The microscopy study was able to shown the intimacy of the interaction between these two phases and provides significant information to establishing its relationship with the activity, selectivity for hydrogen production and stability of the catalysts under reaction conditions. This was further corroborated with additional, conventional TPO and XPS techniques.

The optimum, stable catalytic performance in the glycerol reforming reaction was achieved with a composite system having a 20 mol% of Ni in cation basis. Excess Ni over the 20 mol% is not stabilized by contact with ceria and has thus detrimental effects on catalytic properties. The Ni20 system outperforms the corresponding Ni20/CeO$_2$ reference system prepared by a conventional impregnation method in terms of activity, selectivity as well as stability. Comparison of the literature shows the reaching of an optimum H$_2$/CO$_2$ (7/3) ratio at significantly lower temperatures, being this ratio constant in a long catalytic run (48 h). Consequently, production of by-products like CO and CH$_4$ was kept to a minimum, contrarily to the usual Ni-based reforming catalysts. The outstanding properties of Ni20 would represent a proof of concept for the glycerol reforming reaction.

Acknowledgments

Appendix A. Supplementary data

Supplementary data associated with this article can be found, in the online version, at http://dx.doi.org/10.1016/j.apcatb.2014.10.007.

References

[1] S.A. Chattanathan, S. Adhikari, N. Abdoulmoumine, Renew. Sustain. Energy Rev. 16 (2012) 2366–2372.
[2] N.H. Tran, G.S.K. Kannangara, Chem. Soc. Rev. 42 (2013) 9454–9479.
[3] G.W. Huber, S. Iborra, A. Corma, Chem. Rev. 106 (2006) 4044–4098.
[4] Global Industry Analyst, http://www.strategyr.com/Glycerin Market Report.asp; http://www.strategyr.com/Emulsifiers_Market_Report.asp
[5] A. Basagiannis, X. Verykios, Catal. Today 127 (2007) 256–264.
[6] E. Nikolla, A. Holewinski, J. Schwank, S. Linic, J. Am. Chem. Soc. 128 (2006) 11354–11361.
[7] J.C. Park, J.U. Bang, J. Lee, C.H. Ko, H. Song, J. Mater. Chem. 20 (2010) 1239–1245.
[8] Z. Gong, L. Barrio, S. Agnoli, S.D. Senanayake, J. Evans, A. Kubacka, M. Estrella, J.C. Hanson, A. Martínez-Arias, M. Fernández-García, J.A. Rodriguez, Angew. Chem. Int. Ed. 49 (2010) 9680–9684.
[9] F. Pompeo, G. Sanhori, N.N. Nichio, Int. J. Hydrogen Energy 35 (2010) 8912–8920.
[10] N. Luo, K. Ouyang, F. Cao, T. Xiao, Biomass Bioenergy 34 (2010) 489–495.
[11] C. Pirez, M. Capron, H. Jobic, F. Dumeignil, L. Jalowiecki-Duhamel, Angew. Chem. Int. Ed. 50 (2011) 10193–10197.
[12] J. Guo, C. Xie, K. Lee, N. Guo, J.T. Miller, M. Janik, C. Song, ACS Catal. 1 (2011) 574.
[13] S.M. Kim, S.I. Wo, ChemSusChem 5 (2012) 1513–1522.
[14] L. Li, S. He, Y. Song, J. Zhao, W. Ji, C.-T. Au, J. Catal. 288 (2012) 54.
[15] S. Li, C. Zhang, G. Wu, J. Gong, Chem. Commun. 49 (2013) 4226–4228.
[16] C. Zhang, H. Yue, Z. Huang, G. Wu, S. Li, X. Ma, J. Gong, ACS Sustain. Chem. Eng. 1 (2013) 161–168.
[17] G. Wu, C. Zhang, S. Li, Z. Han, T. Wang, X. Ma, J. Gong, ACS Sustain. Chem. Eng. 1 (2013) 1052–1062.
[18] R. Trane-Restrup, S. Dahl, A.D. Jensen, Int. J. Hydrogen Energy 38 (2013) 15105–15118.
[19] F. Fang, C. Pirez, S. Paul, M. Capron, H. Jobic, F. Dumeignil, L. Jalowiecki-Duhamel, ChemCatChem 5 (2013) 2207–2216.
[20] S. Li, C. Zhang, Z. Huang, G. Wu, J. Gong, Chem. Commun. 49 (2013) 4226–4228.
[21] C. Wang, N. Sun, N. Zhao, W. Wei, Y. Zhang, Y. Sun, C. Sun, H. Liu, C.E. Snape, ChemCatChem 6 (2014) 640–648.
[22] M. El Doukkaki, A. Iriondo, J.F. Cambra, I. Gandarias, L. Jalowiecki-Duhamel, F. Dumeignil, P.L. Arias, Appl. Catal. A 474 (2014) 80–91.
[23] J.Y. Liu, W.-N. Su, J. Rich, J.F. Lee, B.-J. Wang, ChemSusChem 7 (2014) 570–576.
[24] J.-F. Dacquin, D. Sellam, C. Batiot-Dupeyrat, A. Tougerti, D. Duprez, S. Royer, ChemSusChem 7 (2014) 631–637.
[25] L. Barrio, A. Kubacka, G. Zhou, M. Estrella, A. Martínez-Arias, J.C. Hanson, M. Fernández-García, J.A. Rodríguez, J. Phys. Chem. C 114 (2010) 12689–12697.
[26] M. Varela, A.R. Lupini, K. Van Bentham, A.Y. Borisevich, M.F. Chrisholm, N. Shibata, E. Abe, S.J. Pennycoook, Annu. Rev. Mater. Res. 35 (2005) 539–569.
[27] A. Le Bail, H. Duroy, J.L. Forquet, Mater. Res. Bull. 23 (1988) 447–453.
[28] G.K. Williamson, W.H. Hall, Acta Metall. 1 (1953) 22–31.
[29] S. Özkara-Aydınoğlu, Int. J. Hydrogen Energy 35 (2010) 12821–12828.
[30] S. Adhikari, S. Fernandeo, A. Haryanto, Energy Fuels 21 (2007) 2306–2310.
[31] B. Zhang, X. Tang, Y. Li, Y. Xu, W. Shen, Int. J. Hydrogen Energy 32 (2007) 2367–2373.
[32] A. Iriondo, L. Barrio, J.F. Cambra, P.L. Arias, M.B. Guemez, M.C. Sánchez-Sánchez, R.M. Navarro, J.L.G. Fierro, Int. J. Hydrogen Energy 35 (2010) 11622–11633.
[33] C.D. Dare, K.K. Pant, Renew. Energy 36 (2011) 3195–3202.
[34] M. Benito, R. Padilla, A. Serrano-Lotina, L. Rodríguez, J. Brey, L. Daza, J. Power Sources 192 (2009) 158–164.
[35] V. Michele, M. Signoretto, F. Menegazzo, A. Gallo, V. Dal Santo, G. Cruciani, G. Cerrato, Appl. Catal. B 111/112 (2012) 225–232.
[36] P. Laksmanan, P.P. Upare, N.-T. Le, Y.K. Hwang, H.R. Kim, J.-S. Chang, Appl. Catal. A 468 (2013) 260–268.
[37] Y.-C. Lin, Int. J. Hydrogen Energy 38 (2013) 2678–2700.
[38] B.C. Miranda, R.J. Chimentao, J.B.O. Santos, F. Gispert-Guirado, J. Llorca, F. Medina, F. López Borillo, J.E. Sueiras, Appl. Catal. B 147 (2014) 464–480.
[39] K.O. Christensen, D. Chen, R. Lodeng, A. Holmen, Appl. Catal. A 314 (2006) 9–22.
[40] Z. Wang, X. Shao, A. Larcher, K. Xie, D. Dong, C.-Z. Li, Catal. Today 216 (2013) 44–49.
[41] C. Zang, N. Sun, N. Zhao, W. Wei, J. Zhang, T. Zhao, Y. Sun, C. Sun, H. Liu, C.E. Snape, ChemCatChem 6 (2014) 640–648.
[42] M.C.J. Bradford, M.A. Vannice, Catal. Rev. Sci. Eng. 41 (1999) 1–42.
[43] S. Tang, L. Ji, J. Lin, H.C. Zeng, K.L. Tan, K. Li, J. Catal. 194 (2000) 424–430.
[44] F. Wang, Y. Li, W. Cai, E. Zhang, X. Zhou, W. Shen, Catal. Today 146 (2009) 31–36.
[45] B. Bachiller-Baeza, C. Mateos-Pedrero, M.A. Soria, A. Guerrero-Ruiz, U. Rodemerck, I. Rodríguez-Ramos, Appl. Catal. B: Environ. 129 (2013) 450–459.
[46] E. Desmoni, G.I. Casella, A. Morone, A.M. Salvi, Surf. Interface Anal. 15 (1990) 627–634.
[47] H. Estrade-Szwarckopf, Carbon 42 (2004) 1713–1724.
[48] L. Guczi, G. Stefler, O. Geszti, I. Sajó, Z. Pászti, A. Trompos, Schay Z., Appl. Catal. B 375 (2010) 236–246.